



Label-free metabolic clustering through unsupervised pixel classification of multiparametric fluorescent images

Giada Bianchetti ^{a, b}, Fabio Ciccarone ^c, Maria Rosa Ciriolo ^d, Marco De Spirito ^{a, b, **, *}, Giovambattista Pani ^{a, e}, Giuseppe Maulucci ^{a, b, *}

^a Fondazione Policlinico Gemelli IRCSS, Rome, Italy

^b Department of Neuroscience, Section of Biophysics, Università Cattolica Del Sacro Cuore, Rome, Italy

^c IRCCS San Raffaele Pisana, Department of Human Sciences and Promotion of the Quality of Life, San Raffaele Roma Open University, Rome, Italy

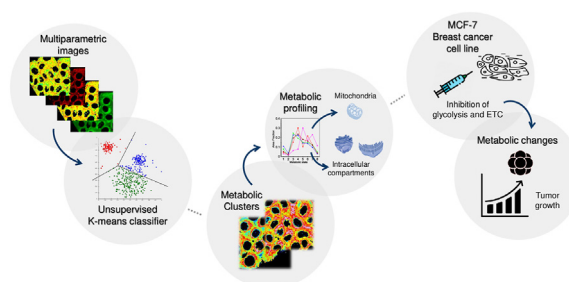
^d Department of Biology, University of Rome Tor Vergata, Rome, Italy

^e Department of Translational Medicine and Surgery, Section of General Pathology, Università Cattolica Del Sacro Cuore, Rome, Italy

HIGHLIGHTS

- An unsupervised learning algorithm detects and classifies metabolic clusters (MC).
- MC are regions having almost uniform metabolic properties.
- MC profile reveals the metabolic activation state of intracellular compartments.
- A contextual label-free detection of mitochondrial turnover is achieved.
- Metabolic changes elicited in the breast cancer cell line MCF-7 are investigated.

GRAPHICAL ABSTRACT



ARTICLE INFO

Article history:

Received 8 August 2020

Received in revised form

21 December 2020

Accepted 22 December 2020

Available online 31 December 2020

Keywords:

Fluorescence lifetime imaging microscopy

Live cell metabolic imaging

Metabolic clustering

NAD(P)H FLIM

Artificial intelligence

Machine learning

ABSTRACT

Autofluorescence microscopy is a promising label-free approach to characterize NADH and FAD metabolites in live cells, with potential applications in clinical practice. Although spectrally resolved lifetime imaging techniques can acquire multiparametric information about the biophysical and biochemical state of the metabolites, these data are evaluated at the whole-cell level, thus providing only limited insights in the activation of metabolic networks at the microscale. To overcome this issue, here we introduce an artificial intelligence-based analysis that, leveraging the multiparametric content of spectrally resolved lifetime images, allows to detect and classify, through an unsupervised learning approach, metabolic clusters, which are regions having almost uniform metabolic properties. This method contextually detects the cellular mitochondrial turnover and the metabolic activation state of intracellular compartments at the pixel level, described by two functions: the cytosolic activation state (CAF) and the mitochondrial activation state (MAF). This method was applied to investigate metabolic changes elicited in the breast cancer cell line MCF-7 by specific inhibitors of glycolysis and electron transport chain, and by the deregulation of a specific mitochondrial enzyme (ACO2) leading to defective aerobic metabolism associated with tumor growth. In this model, mitochondrial fraction undergoes to a 13% increase upon

* Corresponding author. Largo Francesco Vito, 1, 00168, Rome, Italy

** Corresponding author. Fondazione Policlinico Gemelli IRCSS, Rome, Italy.

E-mail addresses: marco.despirito@unicatt.it (M. De Spirito), giuseppe.maulucci@unicatt.it (G. Maulucci).

ACO2 overexpression and the MAF function changes abruptly by altering the metabolic state of about the 25% of the mitochondrial pixels.

© 2020 Elsevier B.V. All rights reserved.

Abbreviations

NAD	Nicotinamide Adenine Dinucleotide	CFP	cyan fluorescent protein
NADP	Nicotinamide Adenine Dinucleotide Phosphate	GFP	green fluorescent protein
FAD	Flavin Adenine Dinucleotide	NA	numerical aperture
CAF	cytosolic activation state	SHG	second harmonic generation
MAF	mitochondrial activation state	ROT	rotenone
ACO2	Aconitase2	RAP	rapamycin
FLIM	fluorescence lifetime imaging microscopy	CTRL	control
ETC	electron transport chain	SA	simulated annealing
DMEM	Dulbecco's Modified Eagle's Medium	AI	artificial intelligence
FBS	fetal bovine serum	WCSS	within-cluster sum of squares
2DG	2-Deoxyglucose	MC	metabolic cluster
		TCA	tricarboxylic acid cycle

1. Introduction

The redox states of the NAD (Nicotinamide Adenine Dinucleotide), NADP (Nicotinamide Adenine Dinucleotide Phosphate) and FAD (Flavin Adenine Dinucleotide) pyridine nucleotide pools play critical roles in defining the activity of energy-producing pathways, in driving oxidative stress and in maintaining antioxidant defenses [1]. NAD and FAD are primarily engaged in regulating energy-producing catabolic processes, whilst NADP is involved in both antioxidant defense and free radical generation. Defects in the balance of these pathways are associated with numerous diseases, from diabetes [2,3] and neurodegenerative disease [4] to heart disease and cancer [5].

Experimentally, the intrinsic fluorescence of the reduced forms of both redox cofactors, NADH and NADPH, has been used to assess the abundance and redox state of these separate pools in living tissues [6,7]. Since NADPH, the phosphorylated form of NADH, cannot spectrally be differentiated from NADH, the convention is to describe the mixed intensity signal as NAD(P)H. NAD(P)H exhibits autofluorescence in its reduced form, whereas NAD(P)⁺ is not fluorescent [8]. This allows microscopic determination of the NAD(P)H redox state by measuring NAD(P)H fluorescence intensity [9]. In particular, the method exploits the autofluorescent properties of the coenzymes NAD(P)H (reduced form of non-fluorescent NAD(P)⁺) and FAD (oxidized form of non-fluorescent FADH₂) for measuring the cellular redox states noninvasively [1,10]. Accordingly, associations with cell metabolism have been demonstrated [11]. This method is powerful since it is a label-free approach and has a general *in-vivo* suitability as demonstrated in numerous tissues such as skeletal muscle [12], brain [13], cochlea [14] and skin [15]. To overcome scattering problems in tissues, Lakowicz et al. employed measurements of NAD(P)H fluorescence lifetime [16]. While free NAD(P)H has a relatively short decay time of about 400 ps, the average fluorescence lifetime of protein-bound NAD(P)H varies between 1.0 and 4.0 ns [17], depending on the enzyme to which it is bound. As the absolute amount of NAD(P)H bound to proteins is relatively stable [18], the ratio of free to protein-bound NAD(P)H is related to the NAD(P)H redox state and to the average NAD(P)H lifetime. Fluorescence Lifetime Imaging Microscopy

(FLIM) expanded the potential of this assay for addressing cell responses in various metabolic diseases and cancer, being able to detect, at pixel resolution, the level of activation of oxidative phosphorylation [14,19–23] as an increase in the fraction of protein-bound NAD. Recently an essay was presented, using one single wavelength (800 nm) to simultaneously acquire spectrally resolved NAD(P)H and FAD FLIM signals, allowing to contextually measure the properties of both metabolites [24].

The cascade of reactions involving several enzymes, sculpturing in a compartmentalized way cell activation profile, can, therefore, be tracked by these FLIM parameters. With this method, however, metabolic states are classified at a whole-cell level, and their uncoupled analysis provides limited insights in the activation of metabolic networks at the microscale [25]. The spectral phasor approaches [26] brought a more complete description of these processes, since it can cluster decay curves without fitting curves with a model, and it was applied also to autofluorescence images [27–29]. The fingerprinting allows for a segmentation of images, but the selection of the clusters depends on the user, who has to select the region to visualize in the phasor plane [30]. This approach is empirical and could lead to biased results. Recently this selection was automatized by a k-means approach [31]. However, the information is not spectrally-resolved and it is based on just two parameters, yielding a limited informative content since it can barely describe the complexity of the intracellular environment. Here, we aimed to improve the label-free spectrally resolved FLIM analysis of both autofluorescent metabolites, by capturing multiparametric information about their concentration and biochemical state, and of the cell activation states they reveal, at a sub-micrometer resolution. Through this technique, each pixel is labelled by four different metabolic parameters: the average lifetime of NADH and FAD, accounting for enzyme specificity and bound fraction of the metabolite, and fluorescence intensity of NADH and FAD, accounting for their concentration. An unsupervised learning clustering tool, leveraging on the multiparametric content of spectrally resolved lifetime images, will detect intracellular metabolic clusters (MC), which are regions having almost uniform metabolic properties [31]. This method, by going beyond the classical whole-cell metabolic classification, provides the quantification of

mitochondrial turnover and of activation states of cytoplasmic and mitochondrial compartments, through the definition of two functions: the cytosolic activation state (CAF) and the mitochondrial activation state (MAF). We applied this method to investigate, in a breast cancer cell line, the metabolic changes triggered by specific inhibitors of glycolysis and electron transport chain (ETC), or by deregulation of a specific mitochondrial enzyme (ACO2) involved in the defective aerobic metabolism associated with tumor growth [32].

2. Materials and Methods

2.1. Cell cultures, transfections, and treatments

MCF-7 cells were cultured in Dulbecco's Modified Eagle's Medium (DMEM) (Lonza, Basel, Switzerland), completed with 10% fetal bovine serum (FBS) (EuroClone, Milan, Italy), 10 U/ml Penicillin/Streptomycin (Lonza) and 2 mM L-Glutamine (Lonza). Mycoplasma test was routinely carried out according to protocols from our laboratory. Cells were cultured at 37 °C in a humidified (air - 5% CO₂) incubator. For the establishment of MCF-7 cells stably-overexpressing ACO2 refer to Ref. [32]. Cells were treated with 2-Deoxyglucose (2DG), Rotenone and Rapamycin, according to the following protocols: 45 g/L of 2DG were prepared in PBS and then added to cells in complete medium (dilution 1:10), 2 h before imaging. The stock of 2.5 mM Rotenone was prepared in ethanol. Cells were treated with a 5 µM Rotenone (1:500 ethanol), 2 h before imaging. Rapamycin (1 mM in DMSO) was added directly to cells in complete medium at 200 nM final concentration, 4 h before imaging.

To evaluate the fraction of mitochondria, 2 µl of CellLight™ Reagent BacMam 2.0 Membrane-CFP and CellLight™ Reagent BacMam 2.0 Mitochondria-GFP (Invitrogen, Carlsbad, CA) were added per 10000 cells in media and cells were then incubated overnight (≥16 h) at 37 °C.

2.2. Confocal microscopy and segmentation of mitochondria

For the detection of mitochondria, petri dishes with Membrane-CFP and Mitochondria-GFP labelled cells are placed on the inverted confocal microscope (Nikon A1 MP) equipped with an on-stage incubator (OKOLAB, Pozzuoli, Italy), ensuring a constant temperature T = 37 °C and CO₂ level (5%). Fluorescence images (excitation: 402 nm for CFP and 488 nm for GFP) are collected in 2 separated channels (emission filter: 450/50 nm for the blue channel, 525/50 nm for the green channel) using a 60 × oil-immersion objective (1.4 NA). Internal photon multiplier tubes collect 16 bit, 1024 × 1024-pixel images at 0.063 ms dwell time.

The intensity-based segmentation of mitochondria is obtained through the open-source software ImageJ v1.53C (NIH), by applying the Max-Entropy method (built-in function 'Threshold') to the green channel image (GFP-emission). The outline of cells is isolated from the blue channel (CFP-emission) by applying the 'Find Edges' tool. The quantification of the mitochondrial fraction (central sections of the cells are sampled as reference) is evaluated as the ratio of the number of pixels corresponding to mitochondria ($N_{\text{pixel}_{\text{MITO}}}$) and the total number of pixels identifying intracellular space ($N_{\text{pixel}_{\text{CELL}}}$), according to the following formula:

$$N_{\text{MITO}}(\%) = \frac{N_{\text{pixel}_{\text{MITO}}}}{N_{\text{pixel}_{\text{CELL}}}} \cdot 100 \quad (1)$$

2.3. Fluorescence intensity and ratio microscopy/fluorescence lifetime microscopy for the contextual quantification of bound fraction and lifetime of NADH and FAD, and NADH and FAD levels with a single 800-nm wavelength excitation for NADH and FAD

Autofluorescence intensity images are acquired with a Nikon A1-MP confocal microscope equipped with a 60 × oil-immersion objective (1.4 NA), a 2-photon Ti:Sapphire laser (MAI TAI DEEP SEE EHPDS -007 (2017), Spectra-Physics, Newport Beach, CA) producing <70-fs pulses at a repetition rate of 80 ± 1 MHz (excitation wavelength 800 nm). A PML-SPEC 16 GaAsP (B&H, Germany) multi-wavelength detector (grating part is the No. 77414) coupled to an SPC-830 TCSPC/FLIM device (B&H, Germany) working in FIFO mode is used to collect the decay data. Calibration was performed through the registration of Second Harmonic Generation (SHG) signals registered at several excitation wavelengths, as recommended by the manufacturer. The software used for acquisition is SPCM-64 (B&H, Germany). For image acquisition, the pixel frame size is set to 512 × 512 and the pixel dwell time is 60 µs. Imaging is performed at 37 °C with 5% CO₂ (cage incubator OKOLAB). The average laser power at the sample is maintained at the mW level (~10 mW). Signals are integrated into the wavelength region 425–475 nm for the blue channel ($I_{\text{NAD(P)H}}(t,x,y)$) and 520–580 nm for the green channel ($I_{\text{FAD}}(t,x,y)$). This FLIM imaging protocol allows simultaneous image acquisition with a single 800-nm wavelength excitation for NADH and FAD with negligible SBT [24].

FLIM acquisitions provide for the decay curves, for each pixel. The lifetimes of the bound (τ_b) and the free (τ_f) fractions of NAD(P)H and FAD are retrieved by fitting the data with a two-exponential decay model. The model is a sum of exponential terms, according to the following expression:

$$I(t) = a_b e^{(-t/\tau_b)} + (1 - a_b) e^{(-t/\tau_f)} \quad (2)$$

where a_b and $(1 - a_b)$ represent the bound and the free fractions of the metabolite, respectively. The 'offset' is kept fixed and set to the measured background value of the acquisition system. For each fit, the three parameters are condensed in a single parameter $\bar{\tau} = a_b \tau_b + (1 - a_b) \tau_f$. The FLIM acquisition in the blue channel yields $\bar{\tau}_{\text{NAD(P)H}}$, which increases with the bound fraction of NADH and depends also by the type of the enzyme to which the metabolite is bound. The FLIM acquisition in the green channel yields $\bar{\tau}_{\text{FAD}}$, which, instead, decreases with the bound fraction of FAD and again depends on the type of the enzyme to which the metabolite is bound.

Fluorescence intensities of NADH and FAD are proportional to the fraction of reduced NAD(P)H and oxidized FAD, respectively. Intensities are measured by performing an integration of the decay signal $I(t,x,y)$ in the time window of width 12.5 ns and in the wavelength regions 420–460 nm and 500–560 nm, yielding for each pixel $I_{\text{NAD(P)H}}$ and I_{FAD} . Background values are measured and subtracted for each image, and debris or other aggregates are removed to avoid biases in the analysis. Background values are removed using the software SPC-image NG (B&H) through the function 'Threshold'. This function defines the minimum number of photons in the peak of a fluorescence curve [33]. Pixels with lower photon number are not analyzed by the fitting procedure, therefore suppressing dark pixels. This value is sampled on $n = 100$ curves on the area outside cells (ranging from 5 to 10). Ultimately, $I_{\text{NAD(P)H}}$, I_{FAD} , $\bar{\tau}_{\text{NAD(P)H}}$ and $\bar{\tau}_{\text{FAD}}$ are retrieved for each pixel, yielding information on metabolite concentration and bound state, with some enzyme selectivity.

2.4. K-means method

The *k*-means algorithm [34,35] represents each of the *k* clusters C_j by the mean (or weighted average) C_j of its points (*centroid*). The sum of distances between elements of a set of points and its centroid, expressed through an appropriate distance function, is used as the objective function. We employed the *L2* norm-based objective function, i.e. the sum of the squares of errors between the points and the corresponding centroids, which is equal to the total intracluster variance

$$E(C) = \frac{1}{2} \sum_{j=1:k} \sum_{x_i \in C_j} \|x_i - C_j\|^2 \quad (3)$$

This objective function is minimized in an optimization problem, and, being based on the *L2* norm, has many unique algebraic properties. Indeed, it coincides with pairwise errors,

$$E'(C) = \frac{1}{2} \sum_{j=1:k} \sum_{x_i, y_i \in C_j} \|x_i - y_i\|^2 \quad (4)$$

and with the difference between the total data variance and the intercluster variance. Therefore, cluster separation and cluster tightness are achieved simultaneously when the function is minimized.

k-means iterative optimization consists of two-step major iterations that: (1) reassign all the points to their nearest centroids, and (2) recompute centroids of newly assembled groups. Iterations continue until a stopping criterion is achieved (no reassignments with tolerance $<10^{-5}$). This version, known as Forgy's algorithm [35] works with any *Lp* norm and it does not depend on data ordering. However, the *k*-means algorithm also has certain shortcomings: 1) dependence from the initial guess of centroids; 2) computation of local minima; 3) problem of *k*-selection; 4) sensitivity to outliers.

In the following, we outline a 5-step workflow that we have followed to reduce the extent of these drawbacks for the determination of the optimal clustering:

- 1) *Determination of the optimal set of parameters*: We extract from each pixel a set of parameters, as listed in Materials and Methods (Section 2.3) (a_b , τ_b , τ_f and intensities), which can be clustered by the *k*-means algorithm. A subset of parameters or transformed parameters (through PCA or selection of parameters revealed useful for characterizing metabolic quantities such as redox ratio [19]). The selection criterion was the highest Silhouette value (see point 5 for details) which guarantees the highest compactness of cluster. According to this workflow, the optimal set of parameters selected to guarantee the optimal clustering, which is obtained by calculating the minimum of equation (3) is the unprocessed one (the raw data, a_b , τ_b , τ_f and intensities).
- 2) *Cluster initialization*: To mitigate the effects of cluster initialization, we applied the method suggested by Bradley and Fayyad [36]. First, *k*-means was performed on several small samples of data with a random initial guess. Each of these constructed systems was then used as a potential initialization for a union of all the samples. Centroids of the best system constructed this way were suggested as an intelligent initial guess to ignite the *k*-means algorithm on the full data.
- 3) *Global minimum*: No initialization guarantees a global minimum for *k*-means. This is a general problem in combinatorial optimization, which is tackled by allowing uphill movements and determines the global minimum of a given set of *n*-dimension

functions with constraints using simulated annealing (SA) method [37].

- 4) *Scaling and Outliers*: The parameters are rescaled using as an offset the mean value of the distribution, and as scaling factor αs , where *s* is the standard deviation of the distribution and α a tunable parameter. If the distributions are almost Gaussians, $\alpha > 3$ ensures that more than 99% of the values are considered. This was verified by visual inspection and qq-plots. When there are significant deviations from Gaussians the α factor is adjusted to include at least 99% of values by direct calculation.
- 5) *Determination of the optimal number of clusters*: The optimal number of clusters is determined by the elbow method and validated with the Silhouette method (Fig. S1) [35]. The elbow method consists in the determination of the within-cluster-sum of squared errors (WSS) for different values of *k*, and in the selection of the *k* value for which WSS becomes first starts to diminish. In the plot of WSS-versus-*k*, this is visible as an elbow (Fig. S1). Silhouette is a method to validate consistency within clusters of data. The silhouette value is a measure of how similar an object is to its cluster compared to other clusters. The silhouette ranges from -1 to $+1$, where a high value indicates that the object is well matched to its cluster and poorly matched to neighbouring clusters.

2.5. Statistics

Statistical tests for sets of biological/biophysical data (Figs. 1D, 2D and 4C, 5G) are performed by R (version 3.63) and RStudio v1.3.959 (<https://www.rstudio.com/>). For the statistical analysis of experimental data, we use the stats package. The software to perform image analysis is in LabVIEW 2019 (National Instruments) and additional details on the presented workflow are available upon request. For image quantification, a minimum of *n* = 40 cells per sample is analyzed. Baseline characteristics among groups have been compared with ANOVA for parametric variables. Quartile-quartile plots checked data normality graphically. A comparison between groups' couples has been made with Tukey's Test.

3. Results

3.1. Analysis of pixel-resolved metabolite intensities of MCF-7 cells undergoing different metabolic treatments

In Fig. 1A, $I_{NAD(P)H}$ (green) and I_{FAD} (red) maps of Control MCF-7 cells treated with 2-Deoxyglucose (2DG), Rotenone (ROT), Rapamycin (RAP), and ACO2-overexpressing cells (ACO2) are reported, reflecting pixel-resolved differences in the concentration and redox state of the metabolites.

Image histograms of $I_{NAD(P)H}$ and I_{FAD} maps (Fig. 1B–C) report the fraction of pixels (vertical axis) versus the intensity of the pixels (horizontal axis). The shape of the histograms are not Gaussians, and their mean and standard deviations are reported in Fig. 1D. There is a $I_{NAD(P)H}$ decrease in the average total cellular fluorescence in 2DG, Rotenone, and Rapamycin-treated samples (with $2DG < RAP < ROT < CTRL$) and an increase in ACO2-overexpressing cells. A similar trend can be observed in I_{FAD} values. The interpretation of these values is not straightforward: indeed, it accounts for variations of both cytoplasmic and mitochondrial NAD(P)H values and different mitochondria/cytoplasm organelle fractions. The separation of NAD(P)H contributions between cytoplasmic and mitochondrial compartments is usually obtained by applying a threshold on NAD(P)H intensity images, by assuming that physiological levels of NAD(P)H in mitochondria are higher than in the cytoplasm [38]. However, as can be observed in Fig. 1E, where

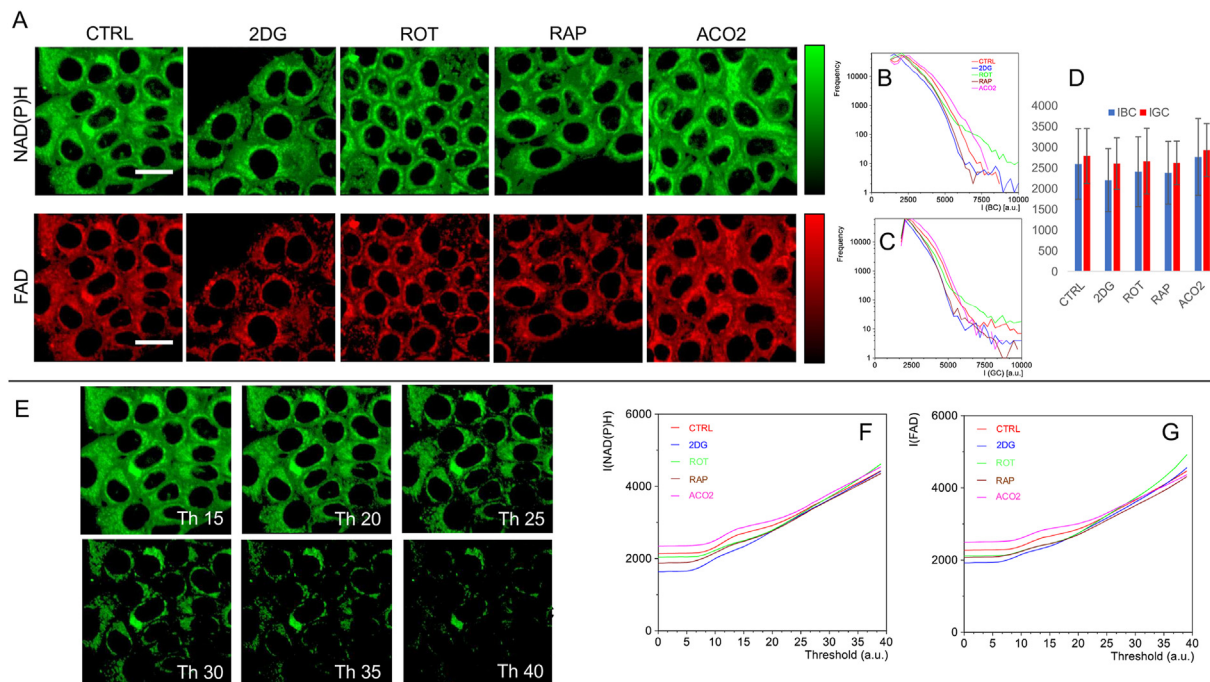


Fig. 1. NAD(P)H and FAD intensity maps of MCF-7 cells undergoing different metabolic treatments. (A) $I_{NAD(P)H}$ (NAD(P)H fluorescence intensity) and I_{FAD} (FAD fluorescence intensity) maps of Control MCF-7 cells, cells treated with 2-Deoxyglucose (2DG), Rotenone (ROT), Rapamycin (RAP), and ACO2-overexpressing MCF-7 cells (ACO2). (B) Image histograms of $I_{NAD(P)H}$ and (C) I_{FAD} , reporting the fraction of pixels (vertical axis, logarithmic scale) versus pixels' intensity (horizontal axis, linear scale) and their (D) mean and standard deviation upon different treatments. (E) NAD(P)H emission maps with increasing values of intensity-based threshold applied to isolate the mitochondrial contribution. Graphs, that report the average intensities of (F) NAD(P)H ($I_{NAD(P)H}$) and (G) FAD (I_{FAD}), show that the relative difference of intensities among the five groups changes as a function of the applied threshold. Intensities and thresholds are reported in auxiliary units. Scale bar is 20 μ m.

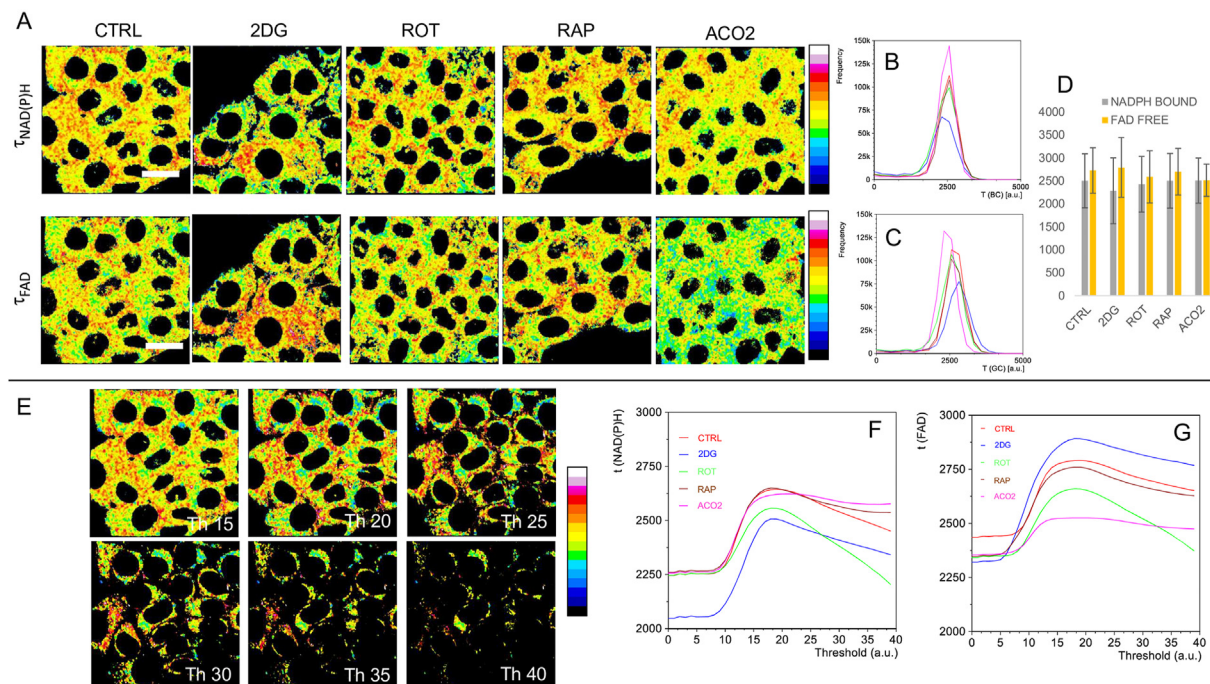


Fig. 2. NAD(P)H and FAD lifetime maps of MCF-7 cells undergoing different metabolic treatments. (A) $\tau_{NAD(P)H}$ (NAD(P)H average fluorescence lifetime) and τ_{FAD} (FAD average fluorescence lifetime) maps of Control MCF-7 cells, cells treated with 2-Deoxyglucose (2DG), Rotenone, Rapamycin, and ACO2-overexpressing MCF-7 cells. (B) Image histograms of $\tau_{NAD(P)H}$ and (C) τ_{FAD} , reporting the fraction of pixels (vertical axis, linear scale) versus pixels' lifetime (horizontal axis, linear scale) and their (D) mean and standard deviation. (E) $\tau_{NAD(P)H}$ maps with increasing values of lifetime-based threshold applied to isolate the mitochondrial contribution. Graphs, that report the average lifetimes of (F) NAD(P)H ($\tau_{NAD(P)H}$) and (G) FAD (τ_{FAD}), show that the relative difference of lifetimes among the five groups changes as a function of the applied threshold. Lifetimes are reported in milliseconds (ms); thresholds are reported in auxiliary units. Scale bar is 20 μ m.

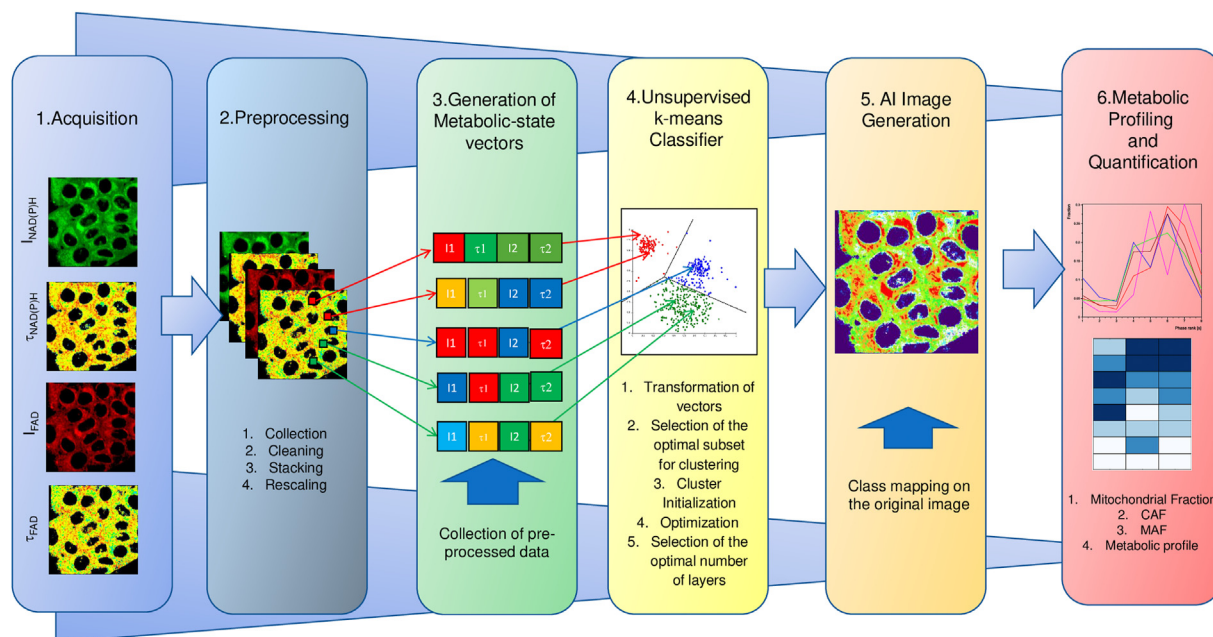


Fig. 3. Workflow for the artificial intelligence clustering of multiparametric autofluorescent images. In the first step (Image Acquisition), multiparametric images are acquired with a hyperspectral imaging system. For each pixel, $I_{NAD(P)H}$, I_{FAD} , $T_{NAD(P)H}$, T_{FAD} are measured. In the second step (preprocessing), images are collected and stacked and data are cleaned and rescaled, creating a multiparametric map in which each pixel is associated with a real metabolic vector $\vec{\phi} = (I_{NAD(P)H}, I_{FAD}, T_{NAD(P)H}, T_{FAD})$ (Step 3, Generation of metabolic state vectors). The dataset of metabolic vectors is sent to a k-means classifier. K-means clustering aims to partition n observations into k clusters in which each observation belongs to the cluster with the nearest mean, serving as a prototype of the cluster. In this step, optimal subsets of metabolic vectors are selected, clusters are initialized, and optimization is performed. The optimal number of cluster is then selected via the Silhouette Method. Each classified pixel is remapped to the pseudo-image (Step 5, AI image generation), that we called the AI image. MC are ranked and pseudo-colored and the computed distribution of the MC is reported in the CAF and MAF functions and in the metabolic-profile graphic plot (Step 6, Metabolic Profile and Quantification).

increasing values of threshold are applied to NAD(P)H intensity maps to isolate the mitochondrial contribution, the optimal separation between the two compartments cannot be easily distinguished. The reason for this resides in the fact that no net intensity variation can be found between the two compartments and some mitochondria with less (or less reduced) metabolite can be exchanged for a cytoplasmic region. To quantify these observations, in Fig. 1F and G the correspondent NAD(P)H ($I_{NAD(P)H}$) and FAD (I_{FAD}) average intensities, evaluated on the increasing thresholded maps, are reported. The graphs show that the relative difference of intensities among the five groups changes as a function of the threshold applied, thus leading to the possible wrong evaluation of both the mitochondrial fraction and the NAD(P)H mitochondrial and cytoplasmic levels. To understand the relevance of this difference, we can observe how in the interval between threshold values 25 and 35, several curves are crossing each other, indicating that a relative decrease of the signal can in principle become a relative increase for some treatments, thus highlighting the need of a data-driven metabolic clustering to properly separate these contributions.

3.2. Analysis of pixel-resolved metabolite lifetimes of MCF-7 cells undergoing different metabolic treatments

In Fig. 2A, $\bar{T}_{NAD(P)H}$ and \bar{T}_{FAD} maps of Control MCF-7, cells treated with 2DG, Rotenone, Rapamycin, and ACO2-overexpressing cells are reported, reflecting pixel-resolved differences in the bound and free fractions and in the lifetimes of the metabolites.

Image histograms of $\bar{T}_{NAD(P)H}$ and \bar{T}_{FAD} maps (Fig. 2B–C) report the fraction of pixels (vertical axis) versus the lifetime of the pixel (horizontal axis). The shapes of the histograms are in this case very symmetric and Gaussian-like, and their mean and standard

deviations are reported in Fig. 2D. There is a $\bar{T}_{NAD(P)H}$ decrease in 2DG, Rotenone, and Rapamycin-treated samples (with $2DG < ROT < RAP < CTRL$) and a slight increase in ACO2-overexpressing cells. \bar{T}_{FAD} increases in 2DG, while a decrease in Rotenone and Rapamycin-treated samples and ACO2-overexpressing cells (with $ACO2 < ROT < RAP < CTRL$) is observed. Again, the interpretation of these values is not straightforward because it includes variations of both cytoplasmic and mitochondrial bound and free fractions, and mitochondria/cytoplasm organelle fraction. Indeed, also in this case, as described in the previous paragraph, the separation of $\bar{T}_{NAD(P)H}$ and \bar{T}_{FAD} contributions between cytoplasmic and mitochondrial compartments via intensity thresholds can lead to user-dependent estimations. As performed for metabolic levels, in Fig. 2E thresholds of increasing values are applied to NAD(P)H intensity maps to isolate the mitochondrial contribution of $\bar{T}_{NAD(P)H}$ and \bar{T}_{FAD} , while in Fig. 2F and G the correspondent NAD(P)H ($I_{NAD(P)H}$) and FAD (I_{FAD}) average intensities calculated on increasing thresholded maps are reported. The graphs show that the relative difference of lifetimes among the five groups changes as a function of the threshold applied, leading to a user-dependent evaluation of both mitochondrial fraction and mitochondrial and cytoplasmic lifetimes of the metabolites. Again, these results highlight the need of a data-driven metabolic clustering that provides for a proper and user-independent separation of these contributions, which will be introduced in the next section.

3.3. Artificial intelligence (AI) clustering of multiparametric autofluorescent images

The distinct analysis of the four maps, while revealing an overall cell response to metabolic perturbation, lacks the specificity needed to fully describe the shift in the level of activation of the

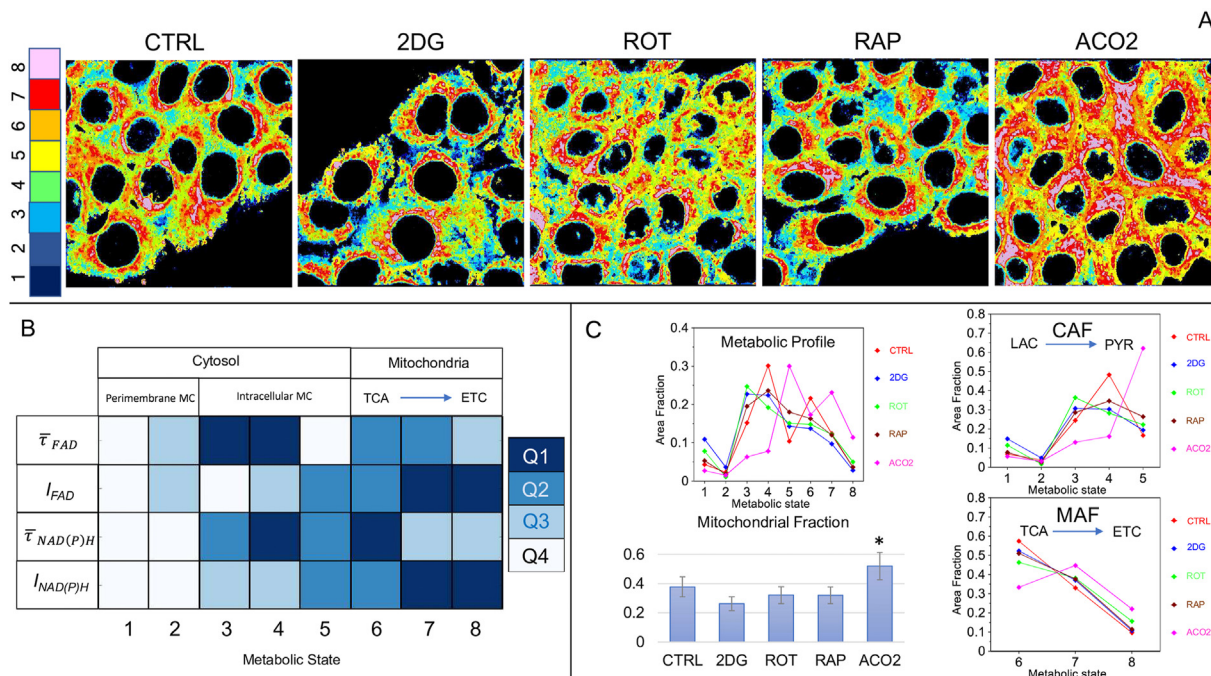


Fig. 4. AI images of MCF-7 Cells. (A) AI images of Control MCF-7, cells treated with 2-Deoxyglucose (2DG), Rotenone, Rapamycin, and ACO2-overexpressing cells. Retrieved classes are labelled with a number in the range 1–8. Class 1 (dark blue) and 2 (indigo) represent background cluster. Class 3–5 represents cytosolic MC. Class 6–8 represents mitochondrial MC. (B) Metabolic cluster characterization by the mean values of ($I_{NAD(P)H}$, I_{FAD} , $\tau_{NAD(P)H}$, τ_{FAD}) calculated on the respective clusters. These values are ranked in four classes (white = fourth quartile-lowest values, light blue = third quartile, blue = second quartile, dark blue = first quartile-highest values). Values of $\tau_{NAD(P)H}$ (average NAD(P)H fluorescence lifetime) range from 1226 to 2837 ps, while τ_{FAD} (average FAD fluorescence lifetime) from 1209 to 2781 ps. (C) The metabolic profile, i.e. a function reporting the area fraction covered by each MC, is reported for each treatment. In the bar plot, the area fraction covered by mitochondria is reported for each treatment. The estimation of mitochondrial fraction allows for the generation of two functions: the cytoplasmic activation function (CAF) and the mitochondrial activation function (MAF). CAF is a function describing the average fraction of the cytoplasmic MC, while MAF is a function describing the average fraction of the mitochondrial MC. The CAF of CTRL cells shows a peak at MC4, while MC3 and MC5 are almost at the same level. Cells treated with 2DG, ROT and RAP have roughly the same CAF. With respect to CTRL cells, the state 4 of treated cells is slightly lower and quite aligned with states 3 and 5. The metabolic profile of ACO2 overexpressing cells is instead very different, with a very high contribution of state 5 (60%) and a concomitant decrease of states 3 and 4. Statistical analysis: ANOVA for parametric variables (* stands for $p < 0.05$; ** stands for $p < 0.01$). Scale bar is 20 μ m.

cytoplasmic and mitochondrial compartments. To extend the spectrum of detectable metabolic state shifts, we applied an AI approach, whose workflow is outlined in Fig. 3.

In the first step, multiparametric images are acquired with a hyperspectral imaging system. For each pixel, four parameters (intensity values and lifetime values for the blue channel (420–490 nm) and the green channel (510–600 nm)) are obtained. In the second step, images are stacked, creating a multiparametric map in which each pixel is associated with a real metabolic vector $\vec{\phi} = (I_{NAD(P)H}, I_{FAD}, \tau_{NAD(P)H}, \tau_{FAD})$. The parameters are then rescaled, and the pixels of the entire dataset analyzed are sent to a k-means classifier (see Section 2.4). K-means clustering aims to partition the n observations into k ($\leq n$) sets $S = \{S_1, S_2, \dots, S_k\}$ to minimize the within-cluster sum of squares (WCSS) (i.e., variance). The obtained cluster center is the representative of its cluster, called the metabolic cluster (MC). The number of observations n corresponds to the total number of pixels analyzed ($n = 512 \times 512 \times m$, where m is the number of images). All the m images of the experiment ($m = 20$, resolution 512×512) are sent to the classifier. In each image from 18 to 22 cells are present. The optimal number of clusters ($k = 9$) is determined by the elbow method and validated with the Silhouette method (see Section 2.4 and Fig. S1). The Silhouette plot displays a local maximum at the chosen $k = 9$ with an average Silhouette value of 0.94 (Fig. S1). Each pixel is classified according to 9 classes, with values going from 0 to 8 (cluster 0 is the trivial cluster (0,0,0,0)), and then remapped to the pseudo-image, that we called AI image. MC are ranked according to the NAD(P)H intensity value. The distribution of MC is calculated by reporting

the fraction of pixels belonging to each class k .

3.4. AI images of MCF-7 cells undergoing different treatment and characterization of the metabolic profile

In Fig. 4A, AI images, obtained as described in Section 3.3, are reported. The retrieved MC, which are regions having relatively uniform metabolic properties, are labelled by a number going from 1 to 8 (excluding the trivial cluster (0,0,0,0)). Each MC is characterized by the mean values of ($I_{NAD(P)H}$, I_{FAD} , $\tau_{NAD(P)H}$, τ_{FAD}), calculated on the respective segmented area. These values, ranked in four classes (white = fourth quartile-lowest values, light blue = third quartile, blue = second quartile, dark blue = first quartile-highest values) are graphically shown in Fig. 4B. MC1 and MC2 correspond to regions in proximity of plasma membrane, with isolated intracellular and perinuclear spots, characterized by the lowest values of both intensity and average lifetimes. MC3 and MC4 represent cytosolic MC, that are characterized by high values of $\tau_{NAD(P)H}$ (Q2 for cluster 3 and Q1 for cluster 4, Fig. 4B) and τ_{FAD} (Q1). Also, MC5, from a visual inspection of the images (yellow pixels), belongs to cytosol. In this cluster however, both $\tau_{NAD(P)H}$ and τ_{FAD} are lower (Q2 and Q4, respectively). MC6, MC7 and MC8 are mitochondrial MC. In these MC, $I_{NAD(P)H}$ and I_{FAD} values are increasingly high, while, in going from 6 to 8, we observe a decrease of both τ_{FAD} and $\tau_{NAD(P)H}$. This trend is associated to an increased FAD binding, and a decreased NADH binding. In Fig. 4C the metabolic profile, i.e., a function reporting the area fraction covered by

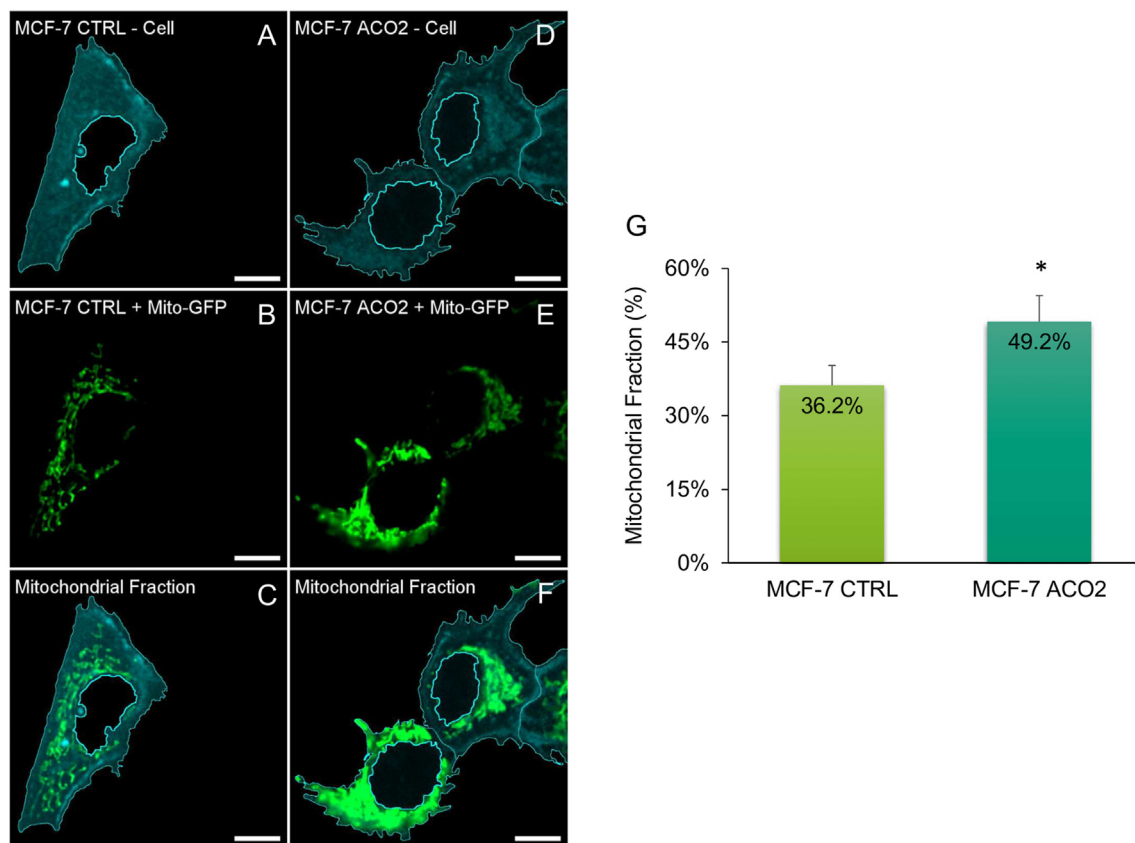


Fig. 5. Average mitochondrial fraction of MCF-7 cells with CFP-labelled membranes and GFP-labelled mitochondria. In (A), the outline and the corresponding intracellular space of Control MCF-7 (CTRL) cells, obtained through an intensity-based segmentation of the blue channel (CFP-emission) is represented. (B) shows the GFP-emission (green channel), corresponding to mitochondria in Control MCF-7. In (C) the overlay of the two contributions, revealing the mitochondrial fraction in CTRL cells, is reported. (D), (E) and (F) show the analogous segmentation for ACO2 overexpressing cells, representing the outline and the corresponding intracellular space (D), the GFP-labelled mitochondria (E) and the overlay (F), respectively. Scale bar is 10 μ m. The average mitochondrial fraction estimated in Control MCF-7 (light green) and ACO2 (dark green) cells ($n = 10$) is reported in the bar plot (G). This fraction, equal to $(36.2 \pm 4.0)\%$ of the whole cell surface in CTRL, significantly increases upon ACO2 overexpression to $(49.2 \pm 5.3)\%$. These values are in agreement with the AI-driven segmentation.

each metabolic cluster, is reported for each treatment. The shape of this function depends not only on the MC equilibrium distribution, but also on mitochondrial area fraction. However, the metabolic state-driven segmentation outlines a criterion for a label-free separation between cytoplasmic and mitochondrial compartments, therefore allowing for an estimation of the area fraction covered by mitochondria (bar plot in Fig. 4C). While in Control and treated cells, the average mitochondrial fraction is constant and equal to $\sim 32\%$ of the whole cell surface, upon ACO2 overexpression, the fraction of mitochondria grows up to $\sim 52\%$. These values are confirmed by an independent experiment in which the spatial distribution of mitochondria labelled with GFP is analyzed (Fig. 5). According to this experiment, the average mitochondrial fraction, that is equal to $(36.2 \pm 4.0)\%$ of the whole cell area in CTRL cells, increases up to $(49.2 \pm 5.3)\%$ in MCF-7 ACO2 cells, as shown in the bar plot reported in Fig. 5G and as recently reported by the authors in the very same cell type [32]. Based on the estimates we obtained, the two measurements are compatible since a T-test does not report a statistically significant difference.

Overall, these observations strongly support the efficiency of our label-free mitochondrial segmentation with respect to intensity-based values obtained with a specific labelling.

The estimation of mitochondrial fraction allows for the generation of two functions: the cytoplasmic activation function (CAF) and the mitochondrial activation function (MAF) (Fig. 4C). CAF is a function describing the average fraction of the cytoplasmic MC,

while MAF is a function describing the average fraction of the mitochondrial MC. The CAF of Control MCF-7 cells shows a peak at MC4, while MC3 and MC5 are almost at the same level. Cells treated with 2DG, ROT and RAP have roughly the same CAF. With respect to CTRL cells, the state 4 of treated cells is slightly lower and quite aligned with states 3 and 5. The metabolic profile of ACO2 overexpressing cells is instead very different, with a very high contribution of MC5 (60%) and a concomitant decrease of MC3 and MC4. MAF of CTRL, 2DG, ROT, and RAP are very similar. They are described by a decreasing function: the relative fraction of MC6, MC7 and MC8 are respectively $\sim 50\%$, $\sim 40\%$ and $\sim 10\%$. Again, the main difference is in the MAF of ACO2 overexpressing cells, which shows a decrease in the proportion of MC6 (30%) and an increase of MC7 (50%) and MC8 (20%).

4. Discussion

The combination of label-free spectrally resolved FLIM analysis of autofluorescent metabolites and the unsupervised learning clustering tool allowed the detection of intracellular MC, i.e., regions having almost uniform metabolic properties. This method, going beyond the classical whole-cell metabolic classification, provided for the quantification of the mitochondrial turnover and the activation states of cytoplasmic and mitochondrial compartments, through the definition of two functions: the cytosolic activation state (CAF) and the mitochondrial activation state (MAF). We

retrieved 8 different MC: classes 1–5 represent cytosolic MC while classes 6–8 represent mitochondrial MC.

The CAF of Control MCF-7 and ACO2 overexpressing cells shows a metabolic transition consisting in a shift from MC4 to MC5. This transition is associated to a metabolic reprogramming of the cytosolic NAD(P)H- and FAD-dependent enzymes. According to the metabolic atlas project [39] more than 200 reactions involve NADH and NAD(P)H in cytosol engaged in carbohydrate lipid, protein and nucleic acid metabolism as well as in transport reactions and 20 involve FAD especially in lipid metabolism and transport reactions. In these settings, we have not enough selectivity to establish an association between lifetime and the set of proteins. We can anyway consider these cluster as functional units of several operating enzymes with a certain grade of activity, which is measured by average lifetimes and intensities. The transition MC4-MC5 observed is associated to the change in lactate production, which is constitutively very high in MCF-7 cells and is subjected to a decrease following the metabolic reprogramming of ACO2 cells. This observation is fully supported by a detailed metabolic characterization of MCF-7 cells and the same ACO2 cell line previously published [32], thus, resulting in a reduction of MC5 fraction. Concomitant processes following ACO2 overexpression and related to the NAD(P)H dependent metabolism of other biomolecules contribute to the observed shift, which is thus not specific to alteration in lactate production. In this view, the MC5 cluster can be associated to compartments representing processes in which glycolysis is channeled to the formation of pyruvate in mitochondria. The CAF of ROT-, 2DG- and RAP-treated cells is quite similar to the one of CTRL cells. This is consistent with the observation that lactate production is enhanced when MCF-7 cells are treated with 2DG [40], and cancer cells are treated with ROT [41] and RAP [42], thus, inducing an analogue metabolic cluster profile. MC1 and MC2 are associated to clusters laying in proximity of the plasma membranes and in isolated intracellular and perinuclear spots, and their fraction is nearly constant. These clusters are characterized by low values of NAD(P)H, FAD and lifetimes, and for their location, can be associated to the activity of NAD(P)H dependent peri-membrane enzymes, such as NADPH oxidase, a membrane-bound enzyme complex that faces the extracellular space, which is expressed in these cells [43].

The mitochondrial MC6-7-8 are instead unchanged with ROT, 2DG and RAP treatments. In these MC, $I_{\text{NAD(P)H}}$ and I_{FAD} values are increasingly high, while, in going from MC6 to MC8, we observe a decrease of both $\tau_{\text{NAD(P)H}}$ and τ_{FAD} . This shift is associated to an increased FAD binding, and a decreased NADH binding. This higher metabolic activity is associated to a higher fraction of free NADH and bound FAD. When Tricarboxylic Acid Cycle (TCA) is active, FAD is bound to succinate dehydrogenase. The increase in bound FAD can be associated to Complex II binding following ETC activation. On these grounds, we therefore associate the increase of MC7-8 to an activation of ETC, concomitantly to TCA. This increase is accompanied to mitochondrial biogenesis, as already shown in Ref. [32] and confirmed by the label-free driven segmentation (Fig. 4) and, independently, by GFP-labelling of mitochondria (Fig. 5). Instead, ETC is nearly inactivated in MCF-7 cells, and also Rotenone, Rapamycin and 2DG treatments are not effective in enhancing ETC activity. Indeed, Rotenone is a direct inhibitor of Complex I, Rapamycin decreases mitochondrial metabolism by inhibition of mTORC1 which lowers mitochondrial membrane potential, oxygen consumption and cellular ATP levels [44,45], while 2DG blocks early steps of glycolysis. To summarize, according to our interpretation and classification, the metabolic shift of the CAF to the high rank cluster values is correlated to a shift in the production from lactate to pyruvate, but the concurrent activation of other

associated metabolic pathways cannot be excluded. A shift of MAF to the high rank cluster values is instead associated to the activation of mitochondrial metabolism from TCA to TCA + ETC state. This method allows also to get insights in the metabolically driven spatial organization of mitochondria in the cell, thus providing for their spatial distribution in relation to their activation state and to the bioenergetic requirements of the cell (Fig. 4A): indeed, MC6 is more peripheral with respect to MC7 and MC8, which instead constitute the core of the mitochondria organelles.

5. Conclusions

In this work, we introduced an artificial intelligence clustering tool that leverages the multiparametric content of spectrally resolved lifetime images, thus resulting in an accurate description of the metabolic processes at a sub-micrometric scale. This method allowed: (1) to reveal that cytosol and mitochondria contain metabolically separated regions in MCF-7 cells, dissecting and characterizing up to six MC, with pixel resolution; (2) to study in real-time metabolic alterations induced by different treatments; (3) to reveal spatial features of the activation state of mitochondria within the mitochondrial network; (4) to provide for a label-free segmentation of mitochondria without relying on inaccurate intensity thresholding. The most original finding in this article is the visualization of MC, which are regions of similar metabolic parameters, rather than regions with uniform chemical structures. These are retrieved by an unsupervised learning technique, which allows to aggregate NAD(P)H and FADH metabolic states as functional units. This method was applied to investigate metabolic changes elicited in the breast cancer cell line MCF-7 by specific inhibitors of glycolysis and electron transport chain, and by the deregulation of the mitochondrial enzyme ACO2 leading to defective aerobic metabolism associated with tumor growth. In this model, we found that mitochondrial fraction undergoes to a 13% increase upon ACO2 overexpression and the MAF function changes abruptly by altering the metabolic state of about the 25% of the mitochondrial pixels. Though powerful since label-free, the method presents as a main drawback the need of a spectrally resolved FLIM system and a two-photon laser. Applications of this technique can have a big impact in the analysis of skin and other epithelial tissues (as colon) through laser scanning endomicroscopes for in vivo cellular and tissue imaging using a Lissajous fiber scanner systems which can be easily implemented with spectrally resolved FLIM acquisition systems, enabling in-vivo diagnosis of tumor formation and development [46]. The artificial intelligence clustering of multiparametric fluorescent images, by allowing the imaging of MC with the sub-micrometric resolution, opens the possibility to deeply investigate mechanisms linking the supramolecular emergent properties to cell functions.

Funding

This work was supported by Università Cattolica del Sacro Cuore Linea D1 2018 grant number R4124500391 (GM) and funded through an EFSD award to GM, supported by EFSD and Sanofi European Pilot Research Grants for Innovative Measurement of Diabetes Outcomes.

CRediT authorship contribution statement

Giada Bianchetti: Methodology, Validation, Formal analysis, Investigation, Data curation, Writing - review & editing, Visualization. **Fabio Ciccarone:** Investigation, Resources, Data curation, Writing - review & editing. **Maria Rosa Ciriolo:** Investigation, Resources, Data curation, Writing - review & editing. **Marco De**

Spirito: Investigation, Resources, Writing - review & editing, Project administration. **Giovambattista Pani:** Investigation, Resources, Writing - review & editing. **Giuseppe Maulucci:** Conceptualization, Methodology, Software, Validation, Formal analysis, Investigation, Resources, Data curation, Writing - original draft, Writing - review & editing, Visualization, Supervision, Project administration, Funding acquisition.

Declaration of competing interest

The authors declare that they have no known competing financial interests or personal relationships that could have appeared to influence the work reported in this paper.

Acknowledgments

The authors acknowledge Mario Amici for his excellent technical support. The authors acknowledge the Cost Action CA15124 “NEUBIAS” for supporting training in image processing and analysis of GB.

Appendix A. Supplementary data

Supplementary data to this article can be found online at <https://doi.org/10.1016/j.aca.2020.12.048>.

References

- [1] G. Maulucci, G. Bačić, L. Bridal, H.H.H.W. Schmidt, B. Tavittian, T. Viel, H. Utsumi, A.S. Yalçın, M. De Spirito, Imaging reactive oxygen species-induced modifications in living systems, *Antioxidants Redox Signal.* 24 (2016) 939–958, <https://doi.org/10.1089/ars.2015.6415>.
- [2] G. Maulucci, E. Cordelli, A. Rizzi, F. De Leva, M. Papi, G. Ciasca, D. Samengo, G. Pani, D. Pitocco, P. Soda, G. Ghirlanda, G. Iannello, M. De Spirito, Phase separation of the plasma membrane in human red blood cells as a potential tool for diagnosis and progression monitoring of type 1 diabetes mellitus, *PLoS One* 12 (2017), e0184109, <https://doi.org/10.1371/journal.pone.0184109>.
- [3] G. Bianchetti, F. Di Giacinto, D. Pitocco, A. Rizzi, G.E. Rizzo, F. De Leva, A. Flex, E. di Stasio, G. Ciasca, M. De Spirito, G. Maulucci, Red blood cells membrane micropolarity as a novel diagnostic indicator of type 1 and type 2 diabetes, *Anal. Chim. Acta X* 3 (2019) 100030, <https://doi.org/10.1016/j.acax.2019.100030>.
- [4] G. Bianchetti, F. Di Giacinto, M. De Spirito, G. Maulucci, Machine-learning assisted confocal imaging of intracellular sites of triglycerides and cholesterol esters formation and storage, *Anal. Chim. Acta* 1121 (2020) 57–66, <https://doi.org/10.1016/j.aca.2020.04.076>.
- [5] W. Ying, NAD⁺/NADH and NADP⁺/NADPH in cellular functions and cell death: regulation and biological consequences, *Antioxidants Redox Signal.* 10 (2008) 179–206, <https://doi.org/10.1089/ars.2007.1672>.
- [6] I. Hassinen, B. Chance, Oxidation-reduction properties of the mitochondrial flavoprotein chain, *Biochem. Biophys. Res. Commun.* 31 (1968) 895–900, [https://doi.org/10.1016/0006-291X\(68\)90536-6](https://doi.org/10.1016/0006-291X(68)90536-6).
- [7] Z. Liu, D. Pouli, C.A. Alonzo, A. Varone, S. Karaliota, K.P. Quinn, K. Mönger, K.P. Karalis, I. Georgakoudi, Mapping metabolic changes by noninvasive, multiparametric, high-resolution imaging using endogenous contrast, *Sci. Adv.* 4 (2018), <https://doi.org/10.1126/sciadv.aap9302>.
- [8] B. Chance, B. Thorell, Localization and assay of respiratory enzymes in single living cells: fluorescence measurements of mitochondrial pyridine nucleotide in aerobiosis and anaerobiosis, *Nature* 184 (1959) 931–934, <https://doi.org/10.1038/184931a0>.
- [9] O.R. Koch, S. Fusco, S.C. Ranieri, G. Maulucci, P. Palozza, L.M. Larocca, A.A.M. Cravero, S.M. Farre', M. De Spirito, T. Galeotti, G. Pani, Role of the life span determinant P66shcA in ethanol-induced liver damage, *Lab. Invest.* 88 (2008) 750–760, <https://doi.org/10.1038/labinvest.2008.44>.
- [10] G. Maulucci, G. Pani, V. Labate, M. Mele, E. Panieri, M. Papi, G. Arcovito, T. Galeotti, M. De Spirito, Investigation of the spatial distribution of glutathione redox-balance in live cells by using Fluorescence Ratio Imaging Microscopy, *Biosens. Bioelectron.* 25 (2009) 682–687, <https://doi.org/10.1016/j.bios.2009.07.038>.
- [11] R.S. Balaban, L.J. Mandel, Metabolic substrate utilization by rabbit proximal tubule. An NADH fluorescence study, *Am. J. Physiol. - Ren. Fluid Electrolyte Physiol.* 254 (1988), <https://doi.org/10.1152/ajprenal.1988.254.3.f407>.
- [12] M.C. Hogan, C.M. Stary, R.S. Balaban, C.A. Combs, NAD(P)H fluorescence imaging of mitochondrial metabolism in contracting *Xenopus* skeletal muscle fibers: effect of oxygen availability, *J. Appl. Physiol.* 98 (2005) 1420–1426, <https://doi.org/10.1152/jappphysiol.00849.2004>.
- [13] T.H. Chia, A. Williamson, D.D. Spencer, M.J. Levene, Multiphoton fluorescence lifetime imaging of intrinsic fluorescence in human and rat brain tissue reveals spatially distinct NADH binding, *Optic Express* 16 (2008) 4237, <https://doi.org/10.1364/oe.16.004237>.
- [14] G. Maulucci, D. Troiani, S.L.M. Eramo, F. Paciello, M.V. Podda, G. Paludetti, M. Papi, A. Maiorana, V. Palmieri, M. De Spirito, A.R. Fetoni, Time evolution of noise induced oxidation in outer hair cells: role of NAD(P)H and plasma membrane fluidity, *Biochim. Biophys. Acta Gen. Subj.* 1840 (2014) 2192–2202, <https://doi.org/10.1016/j.bbagen.2014.04.005>.
- [15] M. Balu, A. Mazhar, C.K. Hayakawa, R. Mittal, T.B. Krasieva, K. König, V. Venugopalan, B.J. Tromberg, In vivo multiphoton NADH fluorescence reveals depth-dependent keratinocyte metabolism in human skin, *Biophys. J.* 104 (2013) 258–267, <https://doi.org/10.1016/j.bpj.2012.11.3809>.
- [16] J.R. Lakowicz, H. Szmajnski, K. Nowaczyk, M.L. Johnson, Fluorescence lifetime imaging of free and protein-bound NADH, *Proc. Natl. Acad. Sci. U. S. A* 89 (1992) 1271–1275, <https://doi.org/10.1073/pnas.89.4.1271>.
- [17] Q. Yu, A.A. Heikal, Two-photon autofluorescence dynamics imaging reveals sensitivity of intracellular NADH concentration and conformation to cell physiology at the single-cell level, *J. Photochem. Photobiol. B Biol.* 95 (2009) 46–57, <https://doi.org/10.1016/j.jphotobiol.2008.12.010>.
- [18] P.M. Schaefer, D. Hilpert, M. Niederschweiberer, L. Neuhauser, S. Kalinina, E. Calzia, A. Rueck, B. von Einem, C.A.F. von Arnim, Mitochondrial matrix pH as a decisive factor in neurometabolic imaging, *Neurophotonics* 4 (2017) 1, <https://doi.org/10.1117/1.nph.4.4.045004>.
- [19] A.J. Walsh, R.S. Cook, H.C. Manning, D.J. Hicks, A. Lafontant, C.L. Arteaga, M.C. Skala, Optical metabolic imaging identifies glycolytic levels, subtypes, and early-treatment response in breast cancer, *Canc. Res.* 73 (2013) 6164–6174, <https://doi.org/10.1158/0008-5472.CAN-13-0527>.
- [20] C. Stringari, R.A. Edwards, K.T. Pate, M.L. Waterman, P.J. Donovan, E. Gratton, Metabolic trajectory of cellular differentiation in small intestine by Phasor Fluorescence Lifetime Microscopy of NADH, *Sci. Rep.* 2 (2012) 568, <https://doi.org/10.1038/srep00568>.
- [21] O.R. Koch, S. Fusco, S.C. Ranieri, G. Maulucci, P. Palozza, L.M. Larocca, A. a M. Cravero, S.M. Farre', M. De Spirito, T. Galeotti, G. Pani, Role of the life span determinant P66(shcA) in ethanol-induced liver damage, *Lab. Invest.* 88 (2008) 750–760, <https://doi.org/10.1038/labinvest.2008.44>.
- [22] S. Fusco, L. Leone, S.A. Barbatì, D. Samengo, R. Piacentini, G. Maulucci, G. Toietta, M. Spinelli, M. McBurney, G. Pani, C. Grassi, A. CREB-sirt1-hes1 circuitry mediates neural stem cell response to glucose availability, *Cell Rep.* 14 (2016) 1195–1205, <https://doi.org/10.1016/j.celrep.2015.12.092>.
- [23] M. Skala, N. Ramanujam, Multiphoton redox ratio imaging for metabolic monitoring in vivo, *Methods Mol. Biol.* 594 (2010) 155–162, https://doi.org/10.1007/978-1-60761-411-1_11.
- [24] R. Cao, H.K. Wallrabe, A. Periasamy, Multiphoton FLIM imaging of NAD(P)H and FAD with one excitation wavelength, *J. Biomed. Optic.* 25 (2020) 1, <https://doi.org/10.1117/1.jbo.25.1.014510>.
- [25] B.P. Yakimov, M.A. Gogoleva, A.N. Semenov, S.A. Rodionov, M.V. Novoselova, A.V. Gayer, A.V. Kovalev, A.I. Bernakevich, V.V. Fadeev, A.G. Armaganov, V.P. Drachev, D.A. Gorin, M.E. Darvin, V.I. Shcheslavskiy, G.S. Budylin, A.V. Priezzhev, E.A. Shirshin, Label-free characterization of white blood cells using fluorescence lifetime imaging and flow-cytometry: molecular heterogeneity and erythrophagocytosis [Invited], *Biomed. Optic Express* 10 (2019) 4220, <https://doi.org/10.1364/boe.10.004220>.
- [26] H. Sediqi, A. Wray, C. Jones, M. Jones, Application of Spectral Phasor analysis to sodium microenvironments in myoblast progenitor cells, *PLoS One* 13 (2018), e0204611, <https://doi.org/10.1371/journal.pone.0204611>.
- [27] H. Szmajnski, V. Toshchakov, J.R. Lakowicz, Application of phasor plot and autofluorescence correction for study of heterogeneous cell population, *J. Biomed. Optic.* 19 (2014), 046017, <https://doi.org/10.1117/1.jbo.19.4.046017>.
- [28] F. Fereidouni, A.N. Bader, A. Colonna, H.C. Gerritsen, Phasor analysis of multiphoton spectral images distinguishes autofluorescence components of in vivo human skin, *J. Biophot.* 7 (2014) 589–596, <https://doi.org/10.1002/jbio.201200244>.
- [29] S. Ranjit, L. Malacrida, M. Stakic, E. Gratton, Determination of the metabolic index using the fluorescence lifetime of free and bound nicotinamide adenine dinucleotide using the phasor approach, *J. Biophot.* 12 (2019), <https://doi.org/10.1002/jbio.201900156>.
- [30] S. Ranjit, R. Datta, A. Dvornikov, E. Gratton, Multicomponent analysis of phasor plot in a single pixel to calculate changes of metabolic trajectory in biological systems, *J. Phys. Chem.* 123 (2019) 9865–9873, <https://doi.org/10.1021/acs.jpca.9b07880>.
- [31] Y. Zhang, T. Hato, P.C. Dagher, E.L. Nichols, C.J. Smith, K.W. Dunn, S.S. Howard, Automatic segmentation of intravital fluorescence microscopy images by K-means clustering of FLIM phasors, *Opt. Lett.* 44 (2019) 3928, <https://doi.org/10.1364/ol.44.003928>.
- [32] F. Ciccarone, L. Di Leo, G. Lazzarino, G. Maulucci, F. Di Giacinto, B. Tavazzi, M.R. Ciriolo, Aconitase 2 inhibits the proliferation of MCF-7 cells promoting mitochondrial oxidative metabolism and ROS/FoxO1-mediated autophagic response, *Br. J. Canc.* 122 (2020) 182–193, <https://doi.org/10.1038/s41416-019-0641-0>.
- [33] W. Becker. The Bh TCSPC Handbook, Becker and Hickl, 2010, pp. 1–566. <http://www.becker-hickl.de/handbook.htm>.
- [34] J.A. Hartigan, M.A. Wong, Algorithm as 136: a K-means clustering algorithm, *Appl. Stat.* 28 (1979) 100, <https://doi.org/10.2307/2346830>.

- [35] J. Kogan, C. Nicholas, M. Teboulle, Grouping Multidimensional Data: Recent Advances in Clustering, Springer Berlin Heidelberg, 2006, <https://doi.org/10.1007/3-540-28349-8>.
- [36] ICML '98: Proceedings of the Fifteenth International Conference on Machine Learning, Morgan Kaufmann Publishers Inc., San Francisco, CA, USA, 1998.
- [37] G.T. Perim, E.D. Wandekokem, F.M. Varejão, K-means initialization methods for improving clustering by simulated annealing | ninfa, lect, Notes Comput. Sci. 133–142 (2008). <http://ninfa.inf.ufes.br/site/en/articles/k-means-initialization-methods-improving-clustering-simulated-annealing>. (Accessed 14 July 2020).
- [38] G.H. Patterson, S.M. Knobel, P. Arkhammar, O. Thastrup, D.W. Piston, Separation of the glucose-stimulated cytoplasmic and mitochondrial NAD(P)H responses in pancreatic islet β cells, Proc. Natl. Acad. Sci. U. S. A 97 (2000) 5203–5207, <https://doi.org/10.1073/pnas.090098797>.
- [39] J.L. Robinson, P. Kocabaş, H. Wang, P.E. Cholley, D. Cook, A. Nilsson, M. Anton, R. Ferreira, I. Domenzain, V. Billa, A. Limeta, A. Hedin, J. Gustafsson, E.J. Kerkhoven, L.T. Svensson, B.O. Palsson, A. Mardinoglu, L. Hansson, M. Uhlén, J. Nielsen, An atlas of human metabolism, Sci. Signal. 13 (2020) 1482, <https://doi.org/10.1126/scisignal.aaz1482>.
- [40] W. Niu, Y. Luo, X. Wang, Y. Zhou, H. Li, H. Wang, Y. Fu, S. Liu, S. Yin, J. Li, R. Zhao, Y. Liu, S. Fan, Z. Li, W. Xiong, X. Li, G. Li, C. Ren, M. Tan, M. Zhou, BRD7 inhibits the Warburg effect and tumor progression through inactivation of HIF1 α /LDHA axis in breast cancer article, Cell Death Dis. 9 (2018) 1–17, <https://doi.org/10.1038/s41419-018-0536-7>.
- [41] Y. Hirata, T. Nagatsu, Rotenone and CCCP inhibit tyrosine hydroxylation in rat striatal tissue slices, Toxicology 216 (2005) 9–14, <https://doi.org/10.1016/j.tox.2005.07.010>.
- [42] M. Khan, D. Biswas, M. Ghosh, S. Mandloi, S. Chakrabarti, P. Chakrabarti, mTORC2 controls cancer cell survival by modulating gluconeogenesis, Cell Death Dis. 1 (2015) 1, <https://doi.org/10.1038/cddiscovery.2015.16>.
- [43] G.H. Lee, S.W. Jin, S.J. Kim, T.H. Pham, J.H. Choi, H.G. Jeong, Tetrabromobisphenol A induces MMP-9 expression via NADPH oxidase and the activation of ROS, MAPK, and Akt pathways in human breast cancer MCF-7 cells, Toxicol. Res. 35 (2019) 93–101, <https://doi.org/10.5487/TR.2019.35.1.093>.
- [44] M. Laplante, D.M. Sabatini, mTOR signaling at a glance, J. Cell Sci. 122 (2009) 3589–3594, <https://doi.org/10.1242/jcs.051011>.
- [45] S.M. Schieke, D. Phillips, J.P. McCoy, A.M. Aponte, R.F. Shen, R.S. Balaban, T. Finkel, The mammalian target of rapamycin (mTOR) pathway regulates mitochondrial oxygen consumption and oxidative capacity, J. Biol. Chem. 281 (2006) 27643–27652, <https://doi.org/10.1074/jbc.M603536200>.
- [46] D.Y. Kim, K. Hwang, J. Ahn, Y.H. Seo, J.B. Kim, S. Lee, J.H. Yoon, E. Kong, Y. Jeong, S. Jon, P. Kim, K.H. Jeong, Lissajous scanning two-photon endomicroscope for in vivo tissue imaging, Sci. Rep. 9 (2019), <https://doi.org/10.1038/s41598-019-38762-w>.